

An Inpainting Approach to Tackle the Kinematic and Thermal SZ Induced Biases in CMB-Cluster Lensing Estimators

**Srinivasan Raghunathan^a Gilbert P. Holder^b James G. Bartlett^{c,d}
SanjayKumar Patil^e Christian L. Reichardt^e Nathan Whitehorn^a**

^aDepartment of Physics and Astronomy, University of California, Los Angeles, CA, USA 90095

^bDepartment of Astronomy and Department of Physics, University of Illinois, 1002 West Green St., Urbana, IL, USA 61801

^cAPC, AstroParticule et Cosmologie, Université Paris Diderot, CNRS/IN2P3, CEA/lrfu, Observatoire de Paris, Sorbonne Paris Cité, 10, rue Alice Domon et Léonie Duquet, Paris Cedex 13, France

^dJet Propulsion Laboratory, California Institute of Technology, 4800 Oak Grove Drive, Pasadena, CA, USA 91109

^eSchool of Physics, University of Melbourne, Parkville, VIC 3010, Australia

E-mail: sri@physics.ucla.edu, gholder@illinois.edu, bartlett@apc.univ-paris7.fr,
s.patil2@student.unimelb.edu.au, christian.reichardt@unimelb.edu.au,
nwhitehorn@physics.ucla.edu

Abstract. A galaxy cluster’s own Sunyaev-Zel’dovich (SZ) signal is known to be a major contaminant when reconstructing the cluster’s underlying lensing potential using cosmic microwave background (CMB) temperature maps. In this work, we develop a modified quadratic estimator (QE) that is designed to mitigate the lensing biases due to the kinematic and thermal SZ effects. The idea behind the approach is to use inpainting to eliminate the cluster’s own emission from the large-scale CMB gradient map. In this inpainted gradient map, we fill the pixel values at the cluster location using a constrained Gaussian realization based on the information from surrounding regions. We show that the noise induced due to inpainting process is small compared to other noise sources for upcoming surveys and has minimal impact on the final lensing signal-to-noise. Without any foreground cleaning, we find a stacked mass uncertainty of 6.5% for the CMB-S4 experiment on a cluster sample containing 5000 clusters with $M_{200c} = 2 \times 10^{14} M_{\odot}$ at $z = 0.7$. In addition to the SZ-induced lensing biases, we also quantify the low mass bias arising due to the contamination of the CMB gradient by the cluster convergence. For the fiducial cluster sample considered in this work, we find that bias is negligible compared to the statistical uncertainties for both the standard and the modified QE even when modes up to $\ell_G \sim 2700$ are used for the gradient estimation. With more gradient modes, we demonstrate that the sensitivity can be increased by 14% compared to the fiducial result above with $\ell_G = 2000$.

Keywords: cosmic background radiation – gravitational lensing:weak – galaxies: clusters: general

Contents

1	Introduction	1
2	Methods	3
2.1	Lensing estimator	3
2.1.1	The quadratic estimator for CMB-cluster lensing	3
2.1.2	Modification to the QE	4
2.2	Simulation set-up	6
3	Results	8
3.1	Baseline results	8
3.1.1	Effect of cluster convergence bias	9
3.1.2	Boosting lensing S/N with more gradient modes	10
3.2	Effect of cluster correlated foregrounds	11
3.2.1	Mock kinematic SZ signal	11
3.2.2	Kinematic SZ from Sehgal simulations	13
3.2.3	Thermal SZ from Sehgal simulations	13
4	Discussion and Conclusion	14

1 Introduction

Galaxy clusters are remarkable cosmological probes, with the caveat that their masses must be accurately measured. In general, cluster masses are not directly measured but estimated from mass-observable scaling relations with observed quantities such as the Sunyaev-Zel'dovich (SZ) fluxes for microwave surveys [1, 2]; galaxy richnesses and galaxy velocities for optical surveys [3–5]; or temperatures of the intra-cluster medium and luminosities for X-ray [6, 7] measurements. The mass precision of these methods has been steadily progressing although challenges remain around that complex astrophysics that relate the survey observables to the underlying dark matter that dominates the cluster mass budget. Once the mass is correctly measured, the abundance of galaxy clusters as a function of redshift and mass can reveal a great deal of information about the cosmological parameters that control the geometry and the growth of structures in the Universe [for a review, see 8].

Weak gravitational lensing can provide an unbiased probe of the matter distribution in a galaxy cluster and arguably yields the best mass estimates. Consequently, several efforts have been made in the last decade to calibrate the mass-observable scaling relations mentioned above using lensing measurements [recently, 9–11]. Weak-lensing measurements can be performed using two background light sources: galaxy or the cosmic microwave background (CMB). While galaxy weak-lensing measurements provide excellent mass constraints for clusters below $z \leq 1$, CMB-cluster lensing is more effective for distant galaxy clusters. Galaxy weak lensing struggles at these high redshifts due to the difficulty in imaging enough background (i.e. even higher redshift) galaxies at sufficient signal-to-noise (S/N). The CMB, in contrast, originates at $z = 1100$ and backlights all galaxy clusters at any redshift. Thus, CMB-cluster lensing is expected to yield the best mass measurements for the thousands of distant galaxy clusters expected to be detected by next generation CMB surveys [12, 13].

Unfortunately though, the lensing S/N for a single cluster is low and one must rely on the stacked mass measurement to achieve a reasonable S/N .

Lensing of the CMB by a galaxy cluster produces a unique dipole pattern that is oriented along the direction of the background CMB gradient at the cluster location. Several estimators have been proposed in the literature [14–22] to extract the lensing signal and the first detections were made by the Atacama Cosmology Telescope (ACT) [23], South Pole Telescope (SPT) [24], and *Planck* [25] experiments. The measurements have flourished since then and have been used to: constrain the hydrostatic mass bias of clusters [25–27]; constrain the optical richness-mass ($\lambda - M$) relation of galaxy clusters [28–30]; and estimate masses of halos hosting high redshift quasars [31].

Lensing measurements using CMB temperature data, however, are highly susceptible to foregrounds, the cluster Sunyaev-Zel’dovich (SZ) signals in particular [32] and previous works have reduced the SZ-biases at the cost of the lensing signal-to-noise (S/N) [24, 29]. In the standard quadratic estimator (sQE), the lensing reconstruction is performed using two maps: the first map to measure the large-scale CMB gradient and the second map to measure the small-scale anisotropies [19]. This estimator leverages the fact that gravitational lensing correlates different angular scales that are uncorrelated in the primordial CMB anisotropy. The real world scenario is complicated by the cluster’s own emission as these foreground signals are also correlated across different angular scales. But given that the lensing signal is oriented along the direction of the background CMB gradient while the foregrounds have no such dependence, it must be possible to decouple the foregrounds from biasing the lensing results.

The most important source of bias is the cluster thermal SZ (tSZ) signal. The tSZ effect is caused because of the interaction between the CMB photons and the hot electrons inside the clusters and has a unique frequency dependence [33]. Recently, Madhavacheril and Hill [34] and Raghunathan *et al.* [30, hereafter R18] used this frequency dependence and modified the quadratic estimator to estimate the background CMB gradient using a tSZ free map. This tSZ-free gradient QE eliminates the tSZ-induced correlation between the two maps, and thus the tSZ bias.

There is also a second SZ effect due to the doppler shifting of CMB photons by the bulk motion of the cluster [35], known as the kinematic SZ (kSZ) effect. While smaller on average than the tSZ effect, the kSZ signal has been observed by several experiments [36–43]. Unfortunately, the kinematic SZ (kSZ) signal can not be removed in the same fashion as the tSZ effect because the kSZ effect has the same blackbody spectrum as the CMB. As a result, the tSZ-free gradient QE mentioned above still suffers from a bias due to the kSZ effect. The bias from kSZ is much smaller than the statistical errors for the current measurements [30] but will be large compared to the statistical uncertainties for cluster lensing measurements with future low noise CMB datasets [32].

Other cluster emission can also bias the CMB-cluster lensing mass measurements. After the SZ effects, the most significant of these are the thermal dust and synchrotron emission from the cluster’s member galaxies. Like the tSZ effect, one might depend on a linear combination of observing frequencies to remove these signals – at the cost of reducing the S/N .

Since the SZ effect and other foregrounds have much smaller polarization fractions than the CMB [44], working with polarization based estimators is another effective way to handle these foreground biases. Polarization estimators have the advantage of simplicity, but are handicapped by the fact that, for CMB experiments over the next decade, the temperature measurements have much higher potential S/N . Another approach is to use the polarization

E/B -mode maps to estimate the background temperature gradient. However, this also reduces the lensing S/N as the correlation between the CMB temperature and polarization fields is $\lesssim 20\%$.

In this work, we design a modified QE that is robust against bias from all types of cluster emission. We focus on the performance with respect to the kSZ and tSZ effect biases, but the scheme should also mitigate dust and radio emission. The idea is to use an inpainted map for the large-scale CMB gradient estimation. We replace the gradient map near the cluster location with the CMB using the information from the surrounding area. Considering that the inpainted CMB gradient map is devoid of the cluster’s SZ, radio and thermal dust emission, there will no longer be foreground-induced correlations between the two maps used in the QE. We also investigate the effect of the SZ signals due to correlated haloes that generally extend beyond the typical cluster size chosen for inpainting. Inpainting also provides a way to estimate the unlensed CMB gradient without being influenced by the cluster’s own convergence field. Hu *et al.* [19] noted that the CMB gradient tended to be underestimated at the cluster location due to the magnification created by the cluster lensing. We show that this approach yields unbiased lensing mass estimates on simulations. The noise introduced from the inpainting process is minimal and we show that it does not affect the lensing S/N .

The paper is organized as follows. The standard quadratic lensing estimator (sQE), its modifications, and a brief description of the inpainting technique are described in §2.1. This is followed by an outline to simulations used to validate the cluster lensing pipeline in §2.2. In §3.1, we compare our estimator to the sQE and tSZ-free gradient estimators, and then quantify the effect of cluster convergence bias. The tests to check robustness of the estimator to SZ-induced lensing biases are in §3.2. We discuss the potential of the estimator with future CMB datasets and conclude in §4. Throughout this work adopt the Λ CDM cosmology obtained from *Planck* 2015 chain that combines the *Planck* 2015 temperature, polarization, lensing power spectra with BAO, H0, and SNe data (TT,TE,EE+lowP+lensing+ext in Table 4 of Planck Collaboration *et al.* [45]).

2 Methods

We introduce the standard lensing quadratic estimator and then present the inpainting technique. This is followed by an overview to the simulations used to validate the lensing pipeline.

2.1 Lensing estimator

2.1.1 The quadratic estimator for CMB-cluster lensing

Gravitational lensing of the CMB remaps the unlensed CMB temperature or polarization fields $\tilde{X}(\hat{\mathbf{n}})$ ($X \in [T, E, B]$) to new positions based on the deflection angle $\alpha(\hat{\mathbf{n}}) = \nabla\phi$ corresponding to the underlying lensing potential ϕ . The total power is conserved by gravitational lensing. Thus, the observed CMB field X at a given position can be written as [46]

$$X(\hat{\mathbf{n}}) = \tilde{X}[\hat{\mathbf{n}} + \nabla\phi(\hat{\mathbf{n}})] \sim \tilde{X}(\hat{\mathbf{n}}) + \nabla\tilde{X}(\hat{\mathbf{n}}) \cdot \nabla\phi(\hat{\mathbf{n}}), \quad (2.1)$$

where we have dropped higher order terms in the Taylor expansion to obtain the expression on the right.

It is convenient to transform the CMB and deflection angle fields to Fourier space, \tilde{X}_ℓ and α_ℓ , where we have used the subscript ℓ to indicate the Fourier transformations. In Fourier

space, lensing convolves the unlensed CMB field \tilde{X}_ℓ and the underlying deflection angle field α_ℓ . Thus, lensing correlates the otherwise independent modes. The basic idea behind the QE is to use these lensing induced correlations to reconstruct the underlying lensing convergence signal $\kappa = -\nabla^2\phi$.

The QE looks at the product of two maps, G and L , to reconstruct the lensing signal [19]:

$$\hat{\kappa}_\ell = -A_\ell \int d^2\hat{\mathbf{n}} e^{-i\hat{\mathbf{n}}\cdot\boldsymbol{\ell}} \text{Re} \{ \nabla \cdot [G(\hat{\mathbf{n}})L^*(\hat{\mathbf{n}})] \}. \quad (2.2)$$

The two maps, which would be independent in the absence of lensing, are both derived from the CMB temperature map T according to:

$$G_\ell = i\ell W_\ell^G T_\ell^G, \quad (2.3)$$

$$L_\ell = W_\ell^L T_\ell^L. \quad (2.4)$$

Here the first map G_ℓ corresponds to a large-scale gradient map while L_ℓ is an optimal weighting of the CMB anisotropy. The notational choice here to distinguish T^G and T^L prefigures the modified versions of the QE; in the original estimator the same temperature map is used for both legs, $T \equiv T^G = T^L$. The optimal linear filters W_ℓ^G and W_ℓ^L are designed to maximize the lensing S/N [19]:

$$W_\ell^G = \begin{cases} C_\ell^{\text{unl}}(C_\ell + N_\ell^G)^{-1}, & \ell \leq \ell_G \\ 0, & \text{otherwise} \end{cases}$$

$$W_\ell^L = (C_\ell + N_\ell^L)^{-1}. \quad (2.5)$$

In the above equation, $(C_\ell^{\text{unl}})C_\ell$ represent the (un)lensed CMB temperature power spectra. In this work, we calculate these spectra using the Code for Anisotropies in the Microwave Background (CAMB¹) [47]. N_ℓ is the beam-deconvolved noise power spectrum for a given map.

Note that in Eq. (2.5), the weight for the gradient modes above ℓ_G are set to zero. This is to minimize the amount by which the CMB gradient at the cluster location is under-estimated due to the magnification of the CMB by the underlying cluster convergence [19]. Henceforth, we will refer to this effect as the *cluster convergence bias*. Since the scales larger than a typical cluster scale (few arcminutes) are relatively unaffected by the convergence signal, the bias can be mitigated by simply removing the more contaminated small-scale modes from the gradient estimation. Subsequently, we set $\ell_G = 2000$ for the fiducial analysis following Hu *et al.* [19]. This heuristic choice of ℓ_G comes from the fact that the small-scale power of the unlensed CMB is exponentially damped [48] and excluding gradient modes $\ell \geq \ell_G$ does not significantly degrade the lensing S/N . We return to this discussion in § 3.1.2 and demonstrate that inpainting allows more modes to be included (and thus better sensitivity) without being affected by the *cluster convergence bias*.

2.1.2 Modification to the QE

As mentioned earlier, the bias due to cluster SZ signals can be mitigated by estimating the background CMB gradient from a tSZ-free CMB map. For example, R18 combined the 95 and 150 GHz channels from the SPTpol experiment to project the tSZ signal from the gradient map. While tSZ-free gradient approach works in principle to eliminate the bias due

¹<https://camb.info/>

to cluster tSZ signal, it is not suitable to remove the lensing induced bias due to cluster kSZ signal as, unlike tSZ, kSZ has no average frequency dependence.

In this work, we follow a different approach and fill the pixel values at the cluster location with the information from the surrounding region using an inpainting technique in the gradient map. This inpainted gradient approach has the following two key merits compared to a tSZ-free gradient. First, the approach can help in mitigating the kSZ-induced lensing bias; and second, the noise and other frequency dependent foregrounds in the gradient map are not enhanced.

Based on Benoit-Lévy *et al.* [49] we define two regions at distances $R \leq R_1$ and $R_1 < R \leq R_2$ from the cluster center. We fill the CMB temperature values T_1 in region R_1 based on the temperature T_2 in R_2 using a constrained Gaussian realization as

$$\hat{T}_1 = \tilde{T}_1 + \hat{\mathbf{C}}_{12} \hat{\mathbf{C}}_{22}^{-1} (T_2 - \tilde{T}_2) \quad (2.6)$$

where \tilde{T}_1, \tilde{T}_2 are the temperature values in the two regions from a random Gaussian realization of the CMB and we use hats to represent the estimated quantities. The above operation is possible since the primordial CMB exhibits coherence over degree scales and the covariance matrix $\hat{\mathbf{C}}_{XY}$ of the CMB fields between two regions X, Y can be calculated using simulations as

$$\hat{\mathbf{C}}_{XY} = \hat{\mathbf{C}}_{YX} = \frac{1}{n-1} \sum_{i=0}^n (\mathbf{G}_i - \langle \mathbf{G} \rangle) (\mathbf{G}_i - \langle \mathbf{G} \rangle)^T \quad (2.7)$$

where the index i runs over the number of simulations and $\mathbf{G} = \begin{pmatrix} \mathbf{G}_X \\ \mathbf{G}_Y \end{pmatrix}$ is the concatenated vector of the Gaussian realization of the large-scale structure (LSS) lensed CMB map in the two regions. The details about our simulations can be found in Raghunathan *et al.* [32] and are discussed briefly in the following section § 2.2.

The effectiveness of the estimator depends on how close the inpainted values \hat{T}_1 are to the true background CMB gradient T_1 . Of course, inpainting introduces extra noise and as expected, the difference between true and inpainted values is higher when the input map is noisier. In addition, the process of inpainting introduces mode mixing and as a result, even though we are only interested in reconstructing the large-scale gradient modes, it is not trivial to avoid the contamination from the noisy small-scale modes. Consequently, we low-pass filter (LPF) the input CMB map T to remove modes $\ell > \ell_{\text{LPF}}$ before performing the inpainting process.

We set $R1 = 4'$ and choose $\ell_{\text{LPF}} \equiv \ell_{\text{LPF},R1} = 2700$ to the scale corresponding to the size of the inpainting radius $R1$. The choice of $\ell_{\text{LPF},R1}$ is well motivated without much S/N penalty given that: (a) no information can be recovered from the inpainted map below the scale corresponding to $R1$; and (b) the small-scale primordial CMB is exponentially damped [48]. The only drawback of the LPF is the undesired ringing effects in the presence of a bright SZ signal at the cluster location. In §3.2, we describe additional filtering steps in the input CMB map T to attenuate these filtering artifacts and cleanly reconstruct the cluster convergence. The outer region $R2$ is set to $30'$ and we perform 50,000 simulations to estimate the covariance matrices. We have confirmed that increasing $R2$ has negligible impact on our results. An illustration of the inpainting process is given in Fig.1 where the first two panels are the $10' \times 10'$ cutouts from the original and reconstructed signals around the desired region chosen for inpainting. Both the panels have been LPF at $\ell_{\text{LPF},R1}$ and include signals from

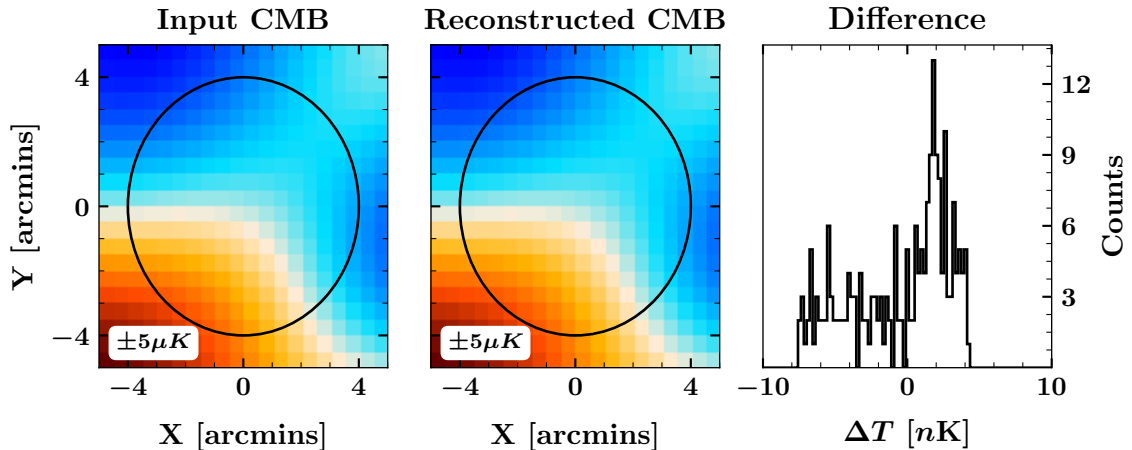


Figure 1. Illustration of the reconstructed CMB temperature using inpainting technique. The first two panels are the $10' \times 10'$ cutouts of the input and the reconstructed signals. They have been LPF at $\ell_{\text{LPF},R1}$ and include signals from CMB, foregrounds, and noise. The black circle is the ($R1 = 4'$) inpainted region. The right panel shows the pixel difference between the two within the inpainted region in nano-Kelvin units.

CMB, foregrounds, and noise. The difference between the two within $R1$ (black circle) is given in the last panel in nano-Kelvin units.

2.2 Simulation set-up

Following the previous work [32], we create Gaussian realizations of the CMB temperature map using the LSS lensed power spectra C_ℓ^{TT} generated using CAMB [47] software for the fiducial *Planck* 2015 cosmology. In these simulations, we neglect the small non-Gaussianities arising due to the lensing from intervening LSS. The simulations are done in the flat-sky approximation and are $120' \times 120'$ wide with a pixel resolution of $0.5'$. The simulations are then lensed using galaxy cluster convergence profiles described below. We add Gaussian realizations of the foregrounds not associated to the galaxy cluster using the measurements made by the SPT-SZ experiment [50]. The foregrounds include dusty and radio galaxy emissions, and the SZ signals from the unresolved haloes in the SPT-SZ 90 and 150 GHz channels. In §3.2, we also include the cluster SZ signals to quantify the level of bias induced in the reconstructed lensing signal. In all cases, the foregrounds remain unlensed by the galaxy cluster. Next, we convolve the simulated maps with a Gaussian beam with $\theta_{\text{FWHM}} = 1.4'$ and add instrumental noise of $\Delta_T = 1.5\mu\text{K}'$ matching the expected configuration² of the wide area survey of the CMB-S4 [12] experiment. For the tSZ-free maps, we set the noise to a slightly higher level $\Delta_T = 4.6\mu\text{K}'$ and use $\theta_{\text{FWHM}} = 2'$. This higher noise level is chosen to match the CMB-S4 tSZ-free map made from the combination of 90 and 150 GHz channels. Adding data from other available channels will tend to reduce the noise level slightly.

To model the galaxy cluster profile, we use the Navarro-Frenk-White (NFW, Navarro

²We use the projected performance of the CMB-S4 150 GHz channel for the Large-area Survey 03 specified in the following link as on 13 March 2019: https://cmb-s4.org/wiki/index.php/Survey_Performance_Expectations#Large-area_Survey_Performance_Expectation_03

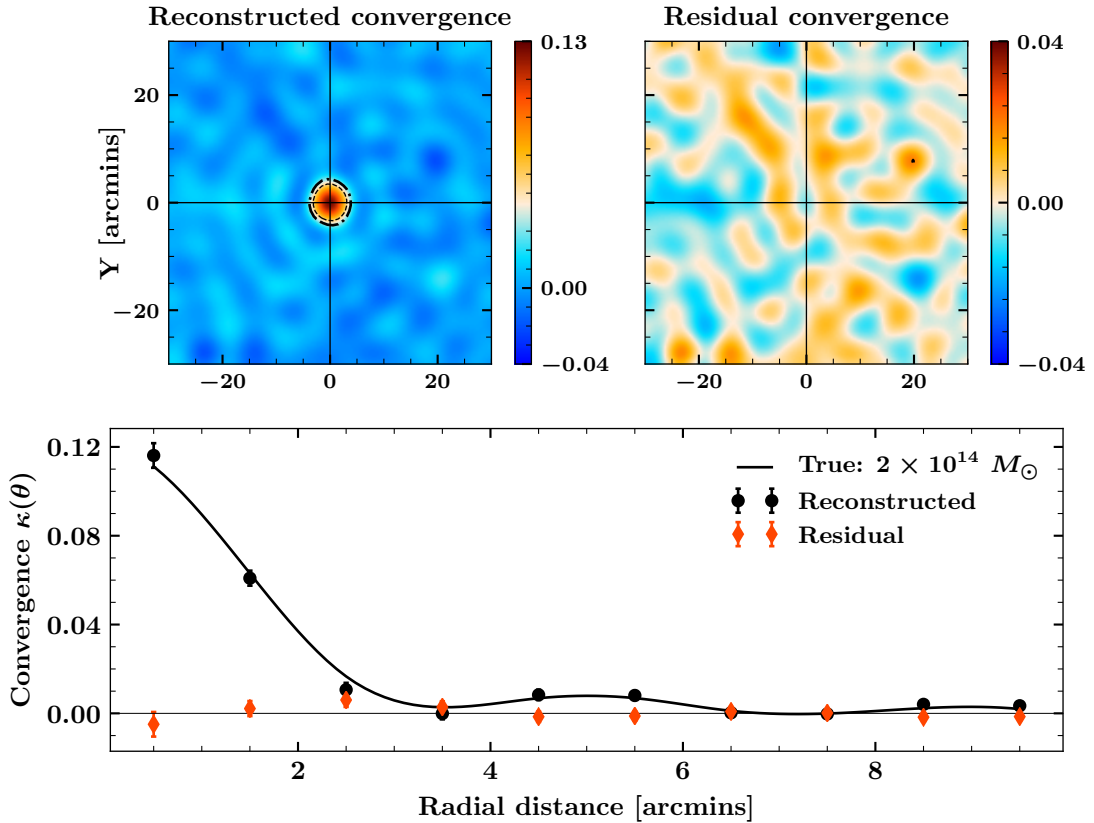


Figure 2. Top left panel shows the reconstructed stacked convergence maps of 5000 clusters using the inpainted gradient estimator. The difference between the true cluster convergence and the left panel is shown in the top right panel. The radially binned reconstructed (black circles), true (black solid curve), and residual (orange diamonds) convergence profiles are in the bottom panel. The residual signal is consistent with a null signal, probability to exceed (PTE) = 0.55, implying that the reconstructed convergence signal is unbiased. The contour lines correspond to regions that are $\geq 3, 5\sigma$ from the background.

et al. 51) formalism given in Eq. (2.8)

$$\rho(r) = \frac{\rho_0}{\left(\frac{r}{R_s}\right) \left(1 + \frac{r}{R_s}\right)^2}, \quad (2.8)$$

where R_s is the scale radius, ρ_0 is the central cluster density, and $c_{200}(M, z) = R_{200}/R_s$ is the halo concentration parameter. To obtain the NFW convergence profile $\kappa(M, z)$ for the NFW halo, we simply plug in the analytic expression given in Eq. (2.8) of Bartelmann [52]. We quote the cluster masses with respect to the radius R_{200c} which encompasses the region within which the average mass density is 200 times the critical density of the Universe at the cluster redshift z . For simplicity, we fix the cluster masses and redshifts to: $M_{200c} = 2 \times 10^{14} M_\odot$ and $z = 0.7$ with $c_{200} = 3.12$ calculated using Duffy *et al.* [53] formula.

3 Results

In § 3.1, we compare the inpainted gradient to the sQE and tSZ-free gradient followed by a discussion about approaches to improving the lensing S/N . Next, in § 3.2 we quantify the impact of the cluster SZ signals on the reconstructed lensing maps and how they can be mitigated using the inpainted gradient estimator.

Throughout this section, we quote the mass constraints obtained by stacking the reconstructed lensing signal $\hat{\kappa}$ from 5000 galaxy clusters. The data points in Fig. 3 and Fig. 4 are the median values obtained from ten such simulations each with 5000 stacked clusters. We bin the stacked signal into 10 linearly spaced radial bins $\hat{\kappa}(\theta)$ with $\Delta\theta = 1'$. We compare the radially binned $\hat{\kappa}(\theta)$ to the fiducial NFW convergence $\kappa(M, z)$ profiles binned radially into $\kappa(\theta)$ and obtain cluster mass constraints using

$$-2 \ln \mathcal{L}(\hat{\kappa}(\theta)|M) = \sum_{\theta=0}^{10'} [\hat{\kappa}(\theta) - \kappa(\theta)] \hat{\mathbf{C}}^{-1} [\hat{\kappa}(\theta) - \kappa(\theta)]^T \quad (3.1)$$

To obtain the covariance matrix we use a jackknife re-sampling technique as

$$\hat{\mathbf{C}} = \frac{N-1}{N} \sum_{j=1}^{N=1000} [\hat{\kappa}_j(\theta) - \langle \hat{\kappa}(\theta) \rangle] [\hat{\kappa}_j(\theta) - \langle \hat{\kappa}(\theta) \rangle]^T, \quad (3.2)$$

where $\hat{\kappa}_j(\theta)$ is the azimuthally binned stacked convergence of all the clusters in the j^{th} sub-sample and $\langle \hat{\kappa}(\theta) \rangle$ is the ensemble average of all the 1000 sub-samples. For parameter constraints, we sample the likelihood space and report the median mass values and 1σ uncertainties from the 16th and 84th percentiles.

3.1 Baseline results

We show the reconstructed convergence map in Fig. 2 for visual demonstration. The top left panel is the stacked convergence map reconstructed obtained using the inpainted gradient estimator. The top right panel is the different between the true cluster convergence and the left panel. In the bottom panel, we show radial profiles of the true (black curve), reconstructed (black circle), and the residual (orange diamond) convergence signals. The PTE value of the residual signal is 0.55 ($\chi_{\text{null}}^2 = 7.9$ for 9 degrees of freedom) indicating that it is consistent with random fluctuations.

The stacked convergence maps from the three estimators are used to obtain the mass constraints and these are presented in the top panel of Fig. 3 for our baseline analysis: sQE (orange hexagon), tSZ-free gradient (red diamond), and inpainted gradient (black circle). All the three estimators return a cluster mass that is $\leq 0.1\sigma$ from the input mass shown as black dash-dotted line. To allow an easy comparison, we set $\ell_G = 2000$ and restrict the gradient estimation to modes $\ell \leq \ell_G$ in all the three cases. With the assumed experimental configuration and with no foreground cleaning for the 150 GHz channel, we note that the uncertainty in the stacked mass of our cluster sample is roughly $\Delta M/M = 6.5\%$. Since the tSZ-free map has a higher noise ($\Delta_{\mathcal{T}} = 4.5\mu\text{K}'$) compared to the fiducial 150 GHz maps ($\Delta_{\mathcal{T}} = 1.4\mu\text{K}'$), one could expect a slightly worse constraint for the tSZ-free gradient. At a first glance, such a trend is not evident for the fiducial case. However, when more gradient modes are included (bottom panel) we note that the improvement in lensing S/N for the tSZ-free gradient is not as high as the other two cases. We give more details about this in §3.1.2.

Lensing mass constraints

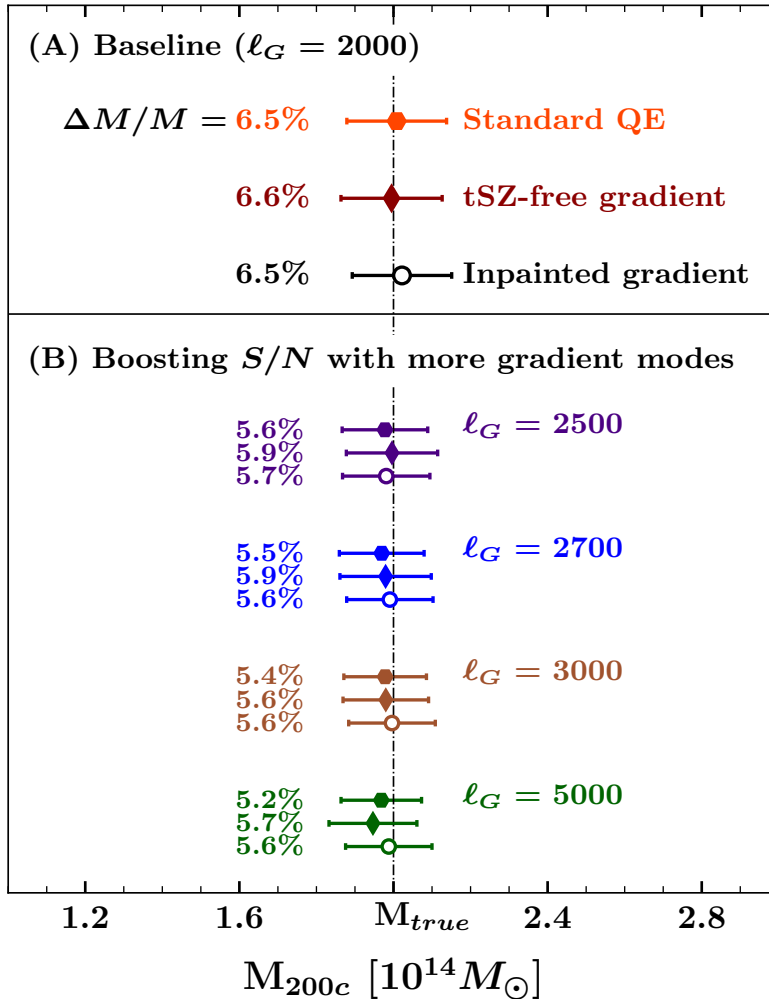


Figure 3. *Top panel:* The mass constraints obtained from the stacked convergence signal for the baseline case ($\ell_G = 2000$) with the sQE (hexagon), tSZ-free gradient (diamond), and inpainted gradient (circle) QE estimators. *Bottom panel:* The improvement in mass precision by including more modes for the gradient estimation. For the inpainted gradient, the S/N saturates after $\ell_G = 2700$ which roughly corresponds to the scale of the inpainting radius $R1 = 4'$.

3.1.1 Effect of cluster convergence bias

Like mentioned in previous sections, the gradient estimation is limited to scales larger than $\ell \leq \ell_G$ for QE in general. This LPF is introduced to mitigate the *cluster convergence bias* arising from an underestimated gradient at the cluster location at the cost of a loss in sensitivity. In this work, we adopt $\ell_G = 2000$ which is reasonable for less massive clusters. But for massive low-redshift clusters which span a larger angular extent on the sky, $\ell_G = 2000$ can leave a mass bias of a few per cent [19]. The goal of this section is to study the effect of the *cluster convergence bias* for different cluster samples and understand if the lensing S/N can be improved without being hit by the bias.

We start this test by investigating the recovered lensing mass from all the three estima-

Table 1. Bias in the reconstructed lensing masses due to the cluster convergence signal. We consider two clusters samples with $M_{200c} = 4 \times 10^{14} M_{\odot}$ at redshifts $z = 0.7$ and $z = 1.5$.

Estimator	ℓ_G	$z = 0.7$		$z = 1.5$	
		Lensing mass [$10^{14} M_{\odot}$]	Bias % (frac. of σ)	Lensing mass [$10^{14} M_{\odot}$]	Bias % (frac. of σ)
Inpainted gradient QE	2700 ($R1 = 4'$)	3.99 ± 0.14	0.2% (0.1σ)	3.96 ± 0.13	1.0% (0.3σ)
	2160 ($R1 = 5'$)	4.01 ± 0.15	0.2% (0.1σ)	3.99 ± 0.14	0.2% (0.1σ)
Standard QE	3000	3.93 ± 0.13	1.8% (0.5σ)	3.81 ± 0.12	4.8% (1.5σ)
	2700	4.04 ± 0.13	1.1% (0.3σ)	3.93 ± 0.12	1.8% (0.6σ)
	2160	4.05 ± 0.15	1.2% (0.3σ)	4.03 ± 0.14	1.1% (0.2σ)

tors for various values of ℓ_G . This is shown in the bottom panel of Fig.3. For the fiducial cluster sample, the effect of the magnification bias on modes $\ell < \ell_G$ is negligible. However, when the value of ℓ_G is increased (2000 through 5000), the recovered mass systematic shifts to a lower value for both sQE (hexagon) and tSZ-free gradient (diamond) points, which is expected to be the *cluster convergence bias*. The inpainted gradient estimator (open circles), which is devoid of the cluster convergence, is not affected and returns an unbiased mass for all values of ℓ_G .

Since the level of bias for sQE and tSZ-free gradient QE is much smaller than the statistical errors, the results are inconclusive. So we extend our analysis to more massive clusters to exaggerate the cluster convergence bias, and measure it in a computationally reasonable sample size. For this test, we use samples of clusters that are $4 \times 10^{14} M_{\odot}$ (i.e. twice as massive as our fiducial sample) at redshifts $z = 0.7$ and $z = 1.5$. The results are presented in Tab. 1. We chose two different radii $R1 = 4'$ and $5'$ for the inpainted gradient estimator and to make fair comparison, set $\ell_G = 2700$ and 2160 corresponding to the scale of $R1$ in the sQE. Our results suggest that the bias due to cluster convergence is smaller than the statistical uncertainty for both the sQE and the inpainted gradient when ℓ_G is set to 2700 or smaller. When $\ell_G \geq 3000$ in sQE, the bias increases and becomes comparable to the statistical errors. These results are consistent with the observations from the Fig.3 for the fiducial cluster sample. For even massive clusters $M_{200c} = 8 \times 10^{14} M_{\odot}$ at $z = 0.7$, the bias is evident. The lensing inferred mass is shifted low by 7% for both the sQE ($\ell_G = 2700$) and inpainted gradient ($R1 = 4'$) estimators. The bias vanishes when $R1$ is set to $8'$ for inpainted gradient or equivalently $\ell_G = 1350$ for sQE with a significant ($\times 1.75$) hit in S/N .

Based on the above results, we conclude that it is safe to set $\ell_G \sim 2700$, when trying to reconstruct the convergence signal from less massive clusters $M_{200c} \sim 2 \times 10^{14} M_{\odot}$, with the next generation datasets without worrying about the convergence bias. The inpainted gradient QE, however, does not have specific advantage over the sQE with respect to the *cluster convergence bias*. The gain in the lensing S/N with a higher ℓ_G is discussed in the next section.

3.1.2 Boosting lensing S/N with more gradient modes

Now that we have an estimate of the *cluster convergence bias*, we could improve the S/N of the estimated convergence by including more modes for the gradient estimation. This improvement is manifested in the bottom panel of Fig. 3 where we show the mass constraints for different values of ℓ_G .

From the figure, it is evident that the S/N increases for all estimators when ℓ_G is set to a higher value. The rate at which the S/N improves and the saturation point, however, differ for the three estimators. When ℓ_G is set to 2500 (purple), we obtain 15% better mass constraint for sQE, 9% for tSZ-free gradient, and 14% for inpainted gradient compared to the fiducial cases in the top panel. The tSZ-free gradient is worse than the other two as the tSZ-free map is noisier than the 150 GHz map. The inpainted gradient is slightly worse than sQE as the inpainting process introduces additional variance. The rate at which the S/N improves is only gradual for even higher ℓ_G due to the diffusion damping of the small-scale CMB [48]. For the inpainted gradient, the S/N finally saturates around $\ell_G \sim 2700$ which corresponds to the scale of the inpainting radius $R1 = 4'$. As expected, the S/N saturates at a higher ℓ_G for both sQE and tSZ-free gradient estimators. Since the tSZ-free gradient map is noisier than the 150 GHz map, the tSZ-free gradient QE attains saturation earlier than the sQE.

3.2 Effect of cluster correlated foregrounds

In this section we study the effect of cluster correlated foregrounds: kSZ and tSZ signal from the galaxy cluster on the standard, tSZ-free gradient, and the inpainted gradient QE. We use $\ell_G = 2700$ for all the tests in this section. First, we inject simple mock kSZ signals followed by realistic foreground signals from Sehgal *et al.* [54, hereafter S10] simulations. To this end, we extract half-arcminute resolution $120' \times 120'$ cutouts from the 90 and 150 GHz kSZ and tSZ S10 simulations around halos corresponding to the cluster sample used here. We scale the tSZ power down from the S10 simulations by a factor of 1.75 to match the George *et al.* [50] measurements. These foreground cutouts are added to our simulated galaxy cluster lensed CMB datasets and processed in the standard manner as discussed in §2.2.

Note that as mentioned in §2.1.2, we LPF the true CMB map at $\ell_{\text{LPF},R1} = 2700$ before the inpainting process to reduce the mode coupling introduced from noisy higher multipoles. This approach works well in the absence of cluster emissions as shown in previous sections. When the cluster emissions are included, particularly tSZ, the LPF can introduce ringing making the inpainting process problematic. There are several known ways of handling this such as, tapering the data with a Hanning window or altering the filter to have a smoother roll-off. In this work, we simply remove an estimate of the SZ signal from the gradient map before the LPF step. We explain this in the subsequent sections below. No such filtering has been performed for the standard or the tSZ-free gradient QE.

3.2.1 Mock kinematic SZ signal

We start by injecting a mock kSZ signal into the simulated CMB maps which is simply a temperature increment $T = T_{\text{CMB}} + T_{\text{kSZ}}$ in the pixels that are within $2'$ from the cluster center. The simulated map is then beam-convolved and processed as in the fiducial case. If unaccounted for, the kSZ signal, which is present in both the maps (G and L), will introduce undesired correlations that are otherwise absent. The inpainted gradient approach with $R1 = 4'$ should encompass this mock kSZ signal and must remain insensitive to it.

To ensure that the LPF step before inpainting does not introduce filtering artifacts, we remove an estimated cluster kSZ signal using the aperture photometry (AP) technique [55, 56]. In this technique, an estimate of \hat{T}_{kSZ} is obtained by computing the difference between the integrated temperature values in two concentric shells $T_{\theta_1} - T_{\theta_2}$ around the cluster where we set $\theta_1 = 1.4'$ and $\theta_2 = \sqrt{2}\theta_1$. This kSZ estimate \hat{T}_{kSZ} is removed from the pixels within θ_1 in the gradient map before the LPF step in the inpainting process. We would like to emphasise

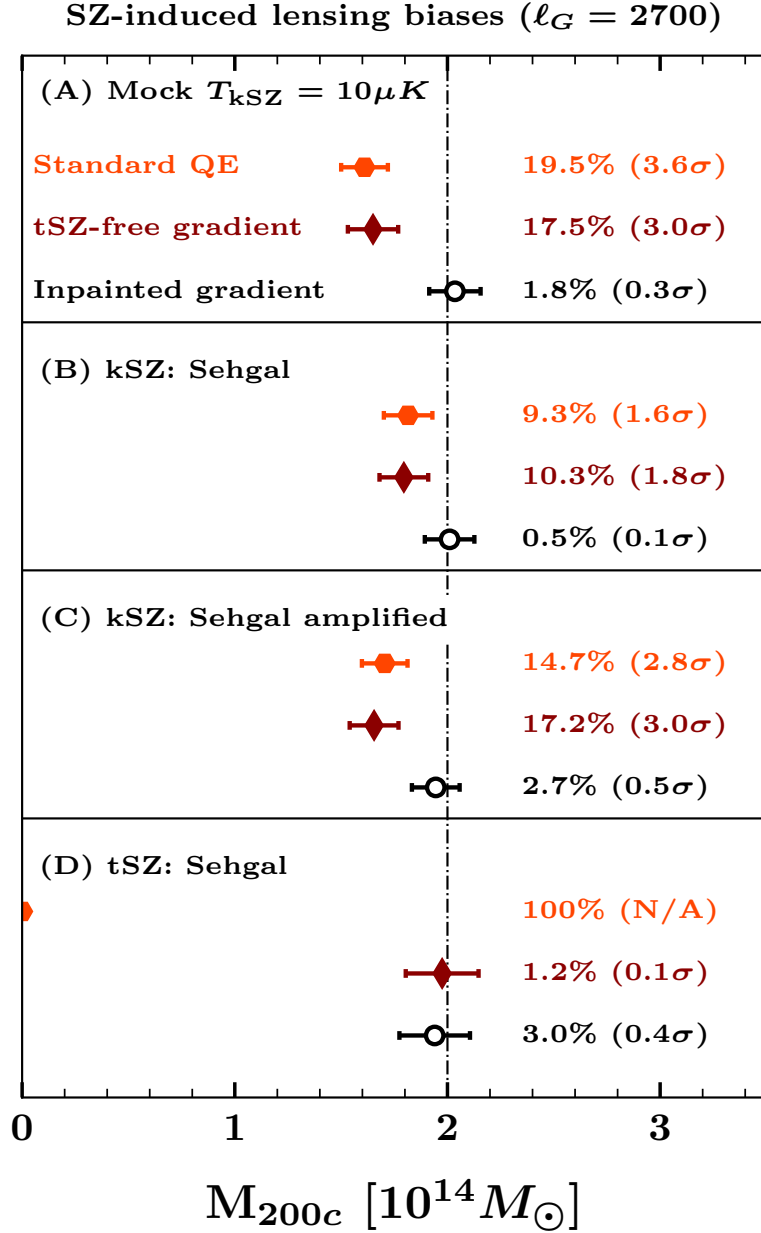


Figure 4. Same as Fig. 3 but after including the cluster SZ signals in the CMB maps. The data points for the standard, tSZ-free gradient, and inpainted gradient are shown as orange hexagons, red diamonds, and black circles. The top three panels are for varying level of kSZ signals: top panel is for a mock kSZ with $T_{\text{kSZ}} = 10\mu\text{K}$; second panel is using kSZ from S10 simulations; third panel also uses S10 simulations but after amplifying them using the signals corresponding to clusters with mass $4 \times 10^{14} M_{\odot}$. In all cases, the inpainted gradient provides an unbiased reconstruction of the cluster mass while the bias in the sQE and tSZ-free gradient grow with the amplitude of the kSZ signal. The bottom panel is for tSZ from S10 simulations. The sQE is heavily biased due to cluster tSZ while the tSZ-free gradient and inpainted gradient are unbiased.

that our goal here is simply to remove a significant portion of the kSZ signal for an efficient inpainting and not to reproduce the true kSZ profiles. As a result, the AP technique serves our purpose well here.

The results of this test are presented in the top panel of Fig. 4. We use $T_{\text{kSZ}} = 10\mu\text{K}$. No noticeable bias is detected for the inpainted gradient while the standard and tSZ-free gradient are biased low by more than 17%. The bias reduces to $\sim 6\%$ when a lower $\ell_G = 2000$ is adopted. The low mass bias in the standard and tSZ-free gradient QE grow with the level of T_{kSZ} and is $> 50\%$ for $T_{\text{kSZ}} = 20\mu\text{K}$. With the inpainted gradient QE, the shift in the reconstructed lensing mass is smaller than the statistical uncertainty ($< 0.4\sigma$) for $T_{\text{kSZ}} = 20\mu\text{K}$. While it is not realistic that all clusters in the sample have such large velocities and consequently a strong kSZ signal, this test serves to emphasise the robustness of the estimator.

3.2.2 Kinematic SZ from Sehgal simulations

In the previous section, we simply modify the temperature of the pixels within $2'$ from the cluster center to input the kSZ signal into the simulated CMB maps. However, it is plausible that the true kSZ profile of the clusters and the correlated haloes has a much wider spread that can extend beyond the inpainting radius $R1$. If this is true, then the kSZ signal outside $R1$ will not only induce kSZ-bias in the lensing reconstruction but also contaminate the inpainting process. To test this case, we use the kSZ signal corresponding to clusters in our sample from the S10 simulations. We repeated this test with an amplified kSZ signal corresponding to clusters that are twice as massive ($M_{200c} = 4 \times 10^{14} M_\odot$). As above, we use the AP technique to remove \hat{T}_{kSZ} in the gradient map before inpainting. These two cases are shown in the second and the third panels of Fig. 4.

As before, the lensing mass from the inpainted gradient remains insensitive to the kSZ signal and the obtained lensing masses are $\leq 0.1\sigma$ and 0.5σ from the true value in the two cases. The lensing mass from the standard and tSZ-free gradient QE are biased low by $\sim 10\%$ in the third panel (3% for $\ell_G = 2000$ instead of 2700) and the bias increases when the kSZ signal is amplified.

When using the kSZ signal from even more massive clusters $M_{200c} \geq 5.9 \times 10^{14} M_\odot$, the lensing mass from the inpainted gradient is low by 7.2% (1.3σ). However, the number of haloes above this mass drops to less than 50 in the S10 simulations and our results could be limited by the sample variance. Nevertheless, the bias becomes much smaller than the statistical error when a larger $R1 = 6'$ is adopted for the inpainting process.

3.2.3 Thermal SZ from Sehgal simulations

In the same spirit, we also checked the effect of tSZ signal from the cluster and correlated haloes [57, 58] that extend outside the inpainting radius $R1$ using S10 simulations. As in the kSZ case, we remove a tSZ estimate from the gradient map before the LPF step in the inpainting process. Given that tSZ is much brighter and extended than the kSZ, we do not rely on a simple AP technique to filter tSZ. Instead, motivated by the work of Patil *et al.* [59], we fit a 2D circular Gaussian model to the cluster tSZ signal and subtract that from the CMB map before the LPF step. The Gaussian model has four free parameters: amplitude, x and y centroids, and the width. Note that we perform this filtering in the gradient G map unlike Patil *et al.* [59] in the L map. While a Gaussian template may not represent the true profile of the cluster tSZ signal, the main objective of the template subtraction is to remove a significant amount of tSZ signal to reduce filtering artifacts from the LPF. We perform the

fitting with the 150 GHz tSZ map that is devoid of CMB by combining the the 90 and 150 GHz channels.

The tSZ tests are presented in the bottom panel of Fig. 4. The sQE, as expected, is heavily biased in the presence of tSZ. Reducing $\ell_G = 2000$ does not help much in the case of tSZ bias for the sQE. On the other hand, the inpainted gradient estimator after removing a Gaussian tSZ model in the gradient map, works well in the even presence of tSZ. We obtain a lensing mass of $M_{\text{lens}} = 1.94 \pm 0.16 \times 10^{14} M_\odot$ consistent with the true cluster mass. If we replace the Gaussian fitting with the AP technique like in the kSZ case, the recovered lensing mass is biased low by 3.5σ for our fiducial inpainting radius $R1 = 4'$. The bias reduces when $R1$ is increased confirming that the tSZ signal outside $4'$ is important. As a further test, we amplified the tSZ signal by injecting signals corresponding to clusters with $M_{200c} = 4 \times 10^{14} M_\odot$. The inpainted gradient returns a lensing mass of $M_{\text{lens}} = 2.18 \pm 0.29 \times 10^{14} M_\odot$ for this case.

For both the above masses, we note that the mass constraints are weakened (8.2% as opposed to 5.6% in Fig.3) when Sehgal tSZ haloes are added to the simulations. As observed previously by R18, this extra variance is due to the presence of the cluster tSZ signal and adjacent haloes (both correlated and uncorrelated haloes in the line-of-sight) in the second leg L of the QE. The residuals from the fitting process also contribute to the excess variance but it is sub-dominant compared to the tSZ signals in the L map. The extra variance can be reduced by removing a matched filter estimate of the tSZ from the second leg for the tSZ-free gradient and inpainted gradient QE as demonstrated by Patil *et al.* [59].

4 Discussion and Conclusion

In this work we have presented a modification to the standard lensing QE by inpainting the large-scale CMB gradient at the cluster location. Using this estimator, we predict that the stacked mass of a cluster sample containing 5000 clusters ($M_{200c} = 2 \times 10^{14} M_\odot$ at $z = 0.7$) can be constrained to $\Delta M/M = 6.5\%$ with a CMB-S4 like low-noise ($\Delta_T = 1.5 \mu\text{K}'$) dataset without performing any foreground cleaning. We compared the estimator to the standard and tSZ-free gradient QE to show that the noise from inpainting is negligible and does not affect the lensing S/N . We also demonstrated that the inpainted gradient QE is robust against lensing biases induced by the cluster kSZ and tSZ signals. In addition to the SZ-induced lensing biases, we have studied the effect of low mass bias arising from the underestimation of the CMB gradient due to the cluster convergence signal. We find that it is safe to use gradient modes up to $\ell \leq \ell_G (= 2700)$ without worrying about the *cluster convergence bias* for the cluster sample considered here. By doing so, we achieve a 14% improvement in the mass constraints compared to the fiducial analysis with $\ell_G = 2000$.

The inpainted gradient estimator presented here will be viable to remove SZ biases for the small-scale cluster lensing reconstruction with the CMB temperature data from the near-term and future CMB experiments. The study about the effect of *cluster convergence bias* performed in this work is also relevant for lensing reconstruction using the polarization data with the future datasets. In addition to the sQE, the inpainting method can also be applied to the tSZ-free gradient and gradient inversion technique [22] for an effective suppression of the kSZ-induced lensing biases.

While not explicitly shown here, the inpainted gradient QE can also be employed to handle the biases due to dust and synchrotron emissions from member galaxies present inside the cluster. But, we leave a careful consideration of these effects to a future work. In addition to the biases considered here, there are other potential systematics that can produce dipole

signals just like the cluster lensing. These are due to (a) the transverse motion of the cluster and correlated haloes referred commonly as the moving-lens effect [18, 60, 61]; and (b) the rotational kSZ because of the rotation of the galaxy cluster [18, 24, 62, 63]. Both these effects may extend outside the inpainting radius. However, in both these cases the direction of the dipole is oriented toward the direction of cluster motion or the rotation, while the CMB-cluster lensing dipole is oriented in the direction of the background CMB gradient. Since the background CMB gradient is not correlated to cluster motion or rotation, the moving-lens effect and the rotational kSZ should average down to zero in the stacked measurements presented here.

The inpainting technique is not limited to cluster lensing and, as demonstrated in an earlier work by Benoit-Lévy *et al.* [49], can also be used to fill the masked regions when reconstructing the CMB lensing power spectrum by the LSS. However, to deal with the SZ-induced biases, from unresolved haloes in particular, for the CMB lensing by LSS the methods prescribed by Madhavacheril and Hill [34], Ferraro and Hill [64], Schaan and Ferraro [65] will yield better results. The tSZ bias can be removed using a tSZ-free gradient gradient QE [34]. The bias from kSZ can be lowered by removing small-scale modes from lensing reconstruction in both legs [64] or just the gradient leg with a degradation in the lensing S/N . Performing the lensing reconstruction using shear estimators is also another novel technique to remain unaffected by the foregrounds biases [65].

Acknowledgements

We are grateful to Nicholas Battaglia, Thomas Crawford, and Emmanuel Schaan for their constructive feedback on the manuscript.

The UCLA authors acknowledge support from NSF grants AST-1716965 and CSSI-1835865. SP acknowledges support from Melbourne International Engagement Award (MIPP) and Laby Travel Bursary. CR acknowledges the support from Australian Research Council's Discovery Projects scheme (DP150103208). This work was performed in the context of the South Pole Telescope scientific program. SPT is supported by the National Science Foundation through grant PLR-1248097. Partial support is also provided by the NSF Physics Frontier Center grant PHY-1125897 to the Kavli Institute of Cosmological Physics at the University of Chicago, the Kavli Foundation and the Gordon and Betty Moore Foundation grant GBMF 947. A part of this research was carried out at the Jet Propulsion Laboratory, California Institute of Technology, under contract with the National Aeronautics and Space Administration. This research used resources of the National Energy Research Scientific Computing Center (NERSC), a DOE Office of Science User Facility supported by the Office of Science of the U.S. Department of Energy under Contract No. DE-AC02-05CH11231. We acknowledge the use of HEALPix [66] and CAMB [47] routines.

References

- [1] L. E. Bleem, B. Stalder, T. de Haan, K. A. Aird, S. W. Allen, D. E. Applegate, M. L. N. Ashby, M. Bautz, M. Bayliss, *et al.*, *The Astrophysical Journal Supplement Series* **216**, 27 (2015), [arXiv:1409.0850 \[astro-ph.CO\]](#) .
- [2] M. Hilton, M. Hasselfield, C. Sifón, N. Battaglia, S. Aiola, V. Bharadwaj, J. R. Bond, S. K. Choi, D. Crichton, R. Datta, *et al.*, *The Astrophysical Journal Supplement Series* **235**, 20 (2018), [arXiv:1709.05600 \[astro-ph.CO\]](#) .

- [3] E. Rozo, R. H. Wechsler, E. S. Rykoff, J. T. Annis, M. R. Becker, A. E. Evrard, J. A. Frieman, S. M. Hansen, J. Hao, D. E. Johnston, B. P. Koester, T. A. McKay, E. S. Sheldon, and D. H. Weinberg, *The Astrophysical Journal* **708**, 645 (2010), [arXiv:0902.3702 \[astro-ph.CO\]](#) .
- [4] A. Saro, J. J. Mohr, G. Bazin, and K. Dolag, *The Astrophysical Journal* **772**, 47 (2013), [arXiv:1203.5708 \[astro-ph.CO\]](#) .
- [5] J. Ruel, G. Bazin, M. Bayliss, M. Brodwin, R. J. Foley, B. Stalder, K. A. Aird, R. Armstrong, M. L. N. Ashby, M. Bautz, *et al.*, *The Astrophysical Journal* **792**, 45 (2014), [arXiv:1311.4953 \[astro-ph.CO\]](#) .
- [6] S. W. Allen, D. A. Rapetti, R. W. Schmidt, H. Ebeling, R. G. Morris, and A. C. Fabian, *MNRAS* **383**, 879 (2008), [arXiv:0706.0033](#) .
- [7] A. Mantz, S. W. Allen, H. Ebeling, D. Rapetti, and A. Drlica-Wagner, *MNRAS* **406**, 1773 (2010), [arXiv:0909.3099 \[astro-ph.CO\]](#) .
- [8] S. W. Allen, A. E. Evrard, and A. B. Mantz, *ARA&A* **49**, 409 (2011), [arXiv:1103.4829 \[astro-ph.CO\]](#) .
- [9] T. McClintock, T. N. Varga, D. Gruen, E. Rozo, E. S. Rykoff, T. Shin, P. Melchior, J. DeRose, S. Seitz, J. P. Dietrich, *et al.*, *MNRAS* **482**, 1352 (2019), [arXiv:1805.00039](#) .
- [10] H. Miyatake, N. Battaglia, M. Hilton, E. Medezinski, A. J. Nishizawa, S. More, S. Aiola, N. Bahcall, J. R. Bond, E. Calabrese, *et al.*, *arXiv e-prints* , [arXiv:1804.05873](#) (2018), [arXiv:1804.05873 \[astro-ph.CO\]](#) .
- [11] J. P. Dietrich, S. Bocquet, T. Schrabback, D. Applegate, H. Hoekstra, S. Grandis, J. J. Mohr, S. W. Allen, M. B. Bayliss, B. A. Benson, *et al.*, *MNRAS* **483**, 2871 (2019), [arXiv:1711.05344 \[astro-ph.CO\]](#) .
- [12] CMB-S4 Collaboration, K. N. Abazajian, P. Adshead, Z. Ahmed, S. W. Allen, D. Alonso, K. S. Arnold, C. Baccigalupi, J. G. Bartlett, N. Battaglia, *et al.*, *ArXiv e-prints* (2016), [arXiv:1610.02743](#) .
- [13] The Simons Observatory Collaboration, P. Ade, J. Aguirre, Z. Ahmed, S. Aiola, A. Ali, D. Alonso, M. A. Alvarez, K. Arnold, P. Ashton, *et al.*, *ArXiv e-prints* (2018), [arXiv:1808.07445](#) .
- [14] U. Seljak and M. Zaldarriaga, *The Astrophysical Journal* **538**, 57 (2000), [astro-ph/9907254](#) .
- [15] S. Dodelson, *Physical Review D*. **70**, 023009 (2004), [arXiv:astro-ph/0402314](#) .
- [16] G. Holder and A. Kosowsky, *The Astrophysical Journal* **616**, 8 (2004), [astro-ph/0401519](#) .
- [17] M. Maturi, M. Bartelmann, M. Meneghetti, and L. Moscardini, *A&A* **436**, 37 (2005), [astro-ph/0408064](#) .
- [18] A. Lewis and A. Challinor, *Phys. Rept.* **429**, 1 (2006), [arXiv:astro-ph/0601594](#) .
- [19] W. Hu, S. DeDeo, and C. Vale, *New Journal of Physics* **9**, 441 (2007), [arXiv:astro-ph/0701276](#) .
- [20] J. Yoo and M. Zaldarriaga, *Physical Review D*. **78**, 083002 (2008), [arXiv:0805.2155](#) .
- [21] J.-B. Melin and J. G. Bartlett, *A&A* **578**, A21 (2015), [arXiv:1408.5633](#) .
- [22] B. Horowitz, S. Ferraro, and B. D. Sherwin, *MNRAS* **485**, 3919 (2019).
- [23] M. Madhavacheril, N. Sehgal, R. Allison, N. Battaglia, J. R. Bond, E. Calabrese, J. Caliguirri, K. Coughlin, D. Crichton, R. Datta, *et al.*, *Physical Review Letters* **114**, 151302 (2015), [arXiv:1411.7999](#) .
- [24] E. J. Baxter, R. Keisler, S. Dodelson, K. A. Aird, S. W. Allen, M. L. N. Ashby, M. Bautz, M. Bayliss, B. A. Benson, L. E. Bleem, *et al.*, *The Astrophysical Journal* **806**, 247 (2015), [arXiv:1412.7521](#) .

- [25] Planck Collaboration, P. A. R. Ade, N. Aghanim, M. Arnaud, M. Ashdown, J. Aumont, C. Baccigalupi, A. J. Banday, R. B. Barreiro, J. G. Bartlett, *et al.*, *A&A* **594**, A24 (2016), [arXiv:1502.01597](#) .
- [26] G. Hurier and R. E. Angulo, *A&A* **610**, L4 (2018), [arXiv:1711.06029 \[astro-ph.CO\]](#) .
- [27] Í. Zubeldia and A. Challinor, arXiv e-prints , [arXiv:1904.07887](#) (2019), [arXiv:1904.07887 \[astro-ph.CO\]](#) .
- [28] J. E. Geach and J. A. Peacock, *Nature Astronomy* **1**, 795 (2017), [arXiv:1707.09369](#) .
- [29] E. J. Baxter, S. Raghunathan, T. M. Crawford, P. Fosalba, Z. Hou, G. P. Holder, Y. Omori, S. Patil, E. Rozo, T. M. C. Abbott, *et al.*, *MNRAS* (2018), [10.1093/mnras/sty305](#), [arXiv:1708.01360](#) .
- [30] S. Raghunathan, S. Patil, E. Baxter, B. A. Benson, L. E. Bleem, T. L. Chou, T. M. Crawford, G. P. Holder, T. McClintock, C. L. Reichardt, *et al.*, *The Astrophysical Journal* **872**, 170 (2019), [arXiv:1810.10998 \[astro-ph.CO\]](#) .
- [31] J. E. Geach, J. A. Peacock, A. D. Myers, R. C. Hickox, M. C. Burchard, and M. L. Jones, arXiv e-prints , [arXiv:1902.06955](#) (2019), [arXiv:1902.06955 \[astro-ph.GA\]](#) .
- [32] S. Raghunathan, S. Patil, E. J. Baxter, F. Bianchini, L. E. Bleem, T. M. Crawford, G. P. Holder, A. Manzotti, and C. L. Reichardt, *JCAP* **8**, 030 (2017), [arXiv:1705.00411](#) .
- [33] R. A. Sunyaev and Y. B. Zel'dovich, *Comments on Astrophysics and Space Physics* **2**, 66 (1970).
- [34] M. S. Madhavacheril and J. C. Hill, *Physical Review D* , 023534 (2018), [arXiv:1802.08230](#) .
- [35] R. A. Sunyaev and Y. B. Zeldovich, *MNRAS* **190**, 413 (1980).
- [36] N. Hand, G. E. Addison, E. Aubourg, N. Battaglia, E. S. Battistelli, D. Bizyaev, J. R. Bond, H. Brewington, J. Brinkmann, B. R. Brown, *et al.*, *Physical Review Letters* **109**, 041101 (2012).
- [37] T. Mroczkowski, S. Dicker, J. Sayers, E. D. Reese, B. Mason, N. Czakon, C. Romero, A. Young, M. Devlin, S. Golwala, *et al.*, *The Astrophysical Journal* **761**, 47 (2012), [arXiv:1205.0052 \[astro-ph.CO\]](#) .
- [38] J. Sayers, T. Mroczkowski, M. Zemcov, P. M. Korngut, J. Bock, E. Bulbul, N. G. Czakon, E. Egami, S. R. Golwala, P. M. Koch, *et al.*, *The Astrophysical Journal* **778**, 52 (2013), [arXiv:1312.3680 \[astro-ph.CO\]](#) .
- [39] J. C. Hill, S. Ferraro, N. Battaglia, J. Liu, and D. N. Spergel, *Physical Review Letters* **117**, 051301 (2016), [arXiv:1603.01608 \[astro-ph.CO\]](#) .
- [40] E. Schaen, S. Ferraro, M. Vargas-Magaña, K. M. Smith, S. Ho, S. Aiola, N. Battaglia, J. R. Bond, F. De Bernardis, E. Calabrese, *et al.*, *Physical Review D* . **93**, 082002 (2016), [arXiv:1510.06442](#) .
- [41] B. Soergel, S. Flender, K. T. Story, L. Bleem, T. Giannantonio, G. Efstathiou, E. Rykoff, B. A. Benson, T. Crawford, S. Dodelson, *et al.*, *MNRAS* **461**, 3172 (2016), [arXiv:1603.03904](#) .
- [42] R. Adam, I. Bartalucci, G. W. Pratt, P. Ade, P. André, M. Arnaud, A. Beelen, A. Benoît, A. Bideaud, N. Billot, *et al.*, *A&A* **598**, A115 (2017), [arXiv:1606.07721 \[astro-ph.CO\]](#) .
- [43] F. De Bernardis, S. Aiola, E. M. Vavagiakis, N. Battaglia, M. D. Niemack, J. Beall, D. T. Becker, J. R. Bond, E. Calabrese, H. Cho, *et al.*, *JCAP* **3**, 008 (2017), [arXiv:1607.02139](#) .
- [44] A. Hall and A. Challinor, *Physical Review D* . **90**, 063518 (2014), [arXiv:1407.5135 \[astro-ph.CO\]](#) .
- [45] Planck Collaboration, P. A. R. Ade, N. Aghanim, M. Arnaud, M. Ashdown, J. Aumont, C. Baccigalupi, A. J. Banday, R. B. Barreiro, J. G. Bartlett, and et al., *A&A* **594**, A13 (2016), [arXiv:1502.01589](#) .

- [46] M. Zaldarriaga and U. Seljak, *Physical Review D.* **59**, 123507 (1999).
- [47] A. Lewis, A. Challinor, and A. Lasenby, *The Astrophysical Journal* **538**, 473 (2000).
- [48] J. Silk, *The Astrophysical Journal* **151**, 459 (1968).
- [49] A. Benoit-Lévy, T. Déchelette, K. Benabed, J. F. Cardoso, D. Hanson, and S. Prunet, *A&A* **555**, A37 (2013), [arXiv:1301.4145 \[astro-ph.CO\]](#) .
- [50] E. M. George, C. L. Reichardt, K. A. Aird, B. A. Benson, L. E. Bleem, J. E. Carlstrom, C. L. Chang, H.-M. Cho, T. M. Crawford, A. T. Crites, *et al.*, *The Astrophysical Journal* **799**, 177 (2015), [arXiv:1408.3161](#) .
- [51] J. F. Navarro, C. S. Frenk, and S. D. M. White, *The Astrophysical Journal* **462**, 563 (1996), [arXiv:astro-ph/9508025](#) .
- [52] M. Bartelmann, *A&A* **313**, 697 (1996), [arXiv:astro-ph/9602053](#) .
- [53] A. R. Duffy, J. Schaye, S. T. Kay, and C. Dalla Vecchia, *MNRAS* **390**, L64 (2008), [arXiv:0804.2486](#) .
- [54] N. Sehgal, P. Bode, S. Das, C. Hernandez-Monteagudo, K. Huffenberger, Y. Lin, J. P. Ostriker, and H. Trac, *The Astrophysical Journal* **709**, 920 (2010), [arXiv:0908.0540](#) .
- [55] Planck Collaboration, P. A. R. Ade, N. Aghanim, M. Arnaud, M. Ashdown, J. Aumont, C. Baccigalupi, A. Balbi, A. J. Banday, R. B. Barreiro, E. Battaner, *et al.*, *A&A* **561**, A97 (2014), [arXiv:1303.5090 \[astro-ph.CO\]](#) .
- [56] D. Alonso, T. Louis, P. Bull, and P. G. Ferreira, *Physical Review D.* **94**, 043522 (2016), [arXiv:1604.01382 \[astro-ph.CO\]](#) .
- [57] V. Vikram, A. Lidz, and B. Jain, *MNRAS* **467**, 2315 (2017), [arXiv:1608.04160 \[astro-ph.CO\]](#) .
- [58] J. C. Hill, E. J. Baxter, A. Lidz, J. P. Greco, and B. Jain, *Physical Review D.* **97**, 083501 (2018), [arXiv:1706.03753 \[astro-ph.CO\]](#) .
- [59] S. Patil *et al.*, In Preparation (2019).
- [60] S. C. Hotinli, J. Meyers, N. Dalal, A. H. Jaffe, M. C. Johnson, J. B. Mertens, M. Münchmeyer, K. M. Smith, and A. van Engelen, *arXiv e-prints* , [arXiv:1812.03167](#) (2018), [arXiv:1812.03167 \[astro-ph.CO\]](#) .
- [61] S. Yasini, N. Mirzaturun, and E. Pierpaoli, *The Astrophysical Journal Letters* **873**, L23 (2019), [arXiv:1812.04241 \[astro-ph.CO\]](#) .
- [62] A. S. Baldi, M. De Petris, F. Sembolini, G. Yepes, W. Cui, and L. Lamagna, *MNRAS* **479**, 4028 (2018), [arXiv:1805.07142 \[astro-ph.CO\]](#) .
- [63] E. J. Baxter, B. D. Sherwin, and S. Raghunathan, *arXiv e-prints* (2019), [arXiv:1904.04199 \[astro-ph.CO\]](#) .
- [64] S. Ferraro and J. C. Hill, *Physical Review D.* **97**, 023512 (2018), [arXiv:1705.06751 \[astro-ph.CO\]](#) .
- [65] E. Schaan and S. Ferraro, *arXiv e-prints* , [arXiv:1804.06403](#) (2018), [arXiv:1804.06403 \[astro-ph.CO\]](#) .
- [66] K. M. Górski, E. Hivon, A. J. Banday, B. D. Wandelt, F. K. Hansen, M. Reinecke, and M. Bartelmann, *The Astrophysical Journal* **622**, 759 (2005), [arXiv:astro-ph/0409513](#) .